



# Enhanced photocatalytic activity of $\text{Bi}_4\text{Ti}_3\text{O}_{12}$ nanosheets by $\text{Fe}^{3+}$ -doping and the addition of Au nanoparticles: Photodegradation of Phenol and bisphenol A

Yongbao Liu<sup>a</sup>, Gangqiang Zhu<sup>a,b,\*</sup>, Jianzhi Gao<sup>a,\*\*</sup>, Mirabbos Hojamberdiev<sup>a</sup>, Runliang Zhu<sup>b,\*\*</sup>, Xiumei Wei<sup>a</sup>, Quanmin Guo<sup>c</sup>, Peng Liu<sup>a</sup>

<sup>a</sup> School of Physics and Information Technology, Shaanxi Normal University, Xi'an, 710062, China

<sup>b</sup> Guangdong Provincial Key Laboratory of Mineral Physics and Materials, Guangzhou Institute of Geochemistry, Guangzhou, 510640, China

<sup>c</sup> School of Physics and Astronomy, University of Birmingham, Edgbaston, Birmingham, B15 2TT, United Kingdom

## ARTICLE INFO

### Article history:

Received 15 January 2016

Received in revised form 23 June 2016

Accepted 28 June 2016

Available online 28 June 2016

### Keywords:

Molten-salt method

Nanosheet

Facet

Plasmonic

Photocatalytic activity

## ABSTRACT

Pure  $\text{Bi}_4\text{Ti}_3\text{O}_{12}$  (BTO) and Fe-doped  $\text{Bi}_4\text{Ti}_3\text{O}_{12}$  (Fe/BTO) nanosheets with exposed {001} facets were synthesized by a one-step molten salt method. Au nanoparticles with a diameter range of 20–50 nm were loaded on 2%Fe-doped  $\text{Bi}_4\text{Ti}_3\text{O}_{12}$  (Au-2%Fe/BTO) nanosheets via a room-temperature hydrogen peroxide reduction method. The UV-vis diffuse reflectance spectra showed that the Fe/BTO and Au-2%Fe/BTO samples exhibit an obvious red shift in visible light absorption band in comparison with the pure BTO. Phenol and bisphenol A solutions were chosen as model organic pollutants to verify the influence of  $\text{Fe}^{3+}$ -doping and plasmonic effect of Au nanoparticles on the photocatalytic activity of the catalyst. The Au-2%Fe/BTO sample exhibited the highest photocatalytic activity compared with other samples. The high photocatalytic activity of Au-2%Fe/BTO rises from two contributions: i) the  $\text{Fe}^{3+}$  ion acts as an efficient scavenger to trap electrons, and hence promotes the separation of photo-induced electron-hole pairs; ii) the visible light response of the catalyst is enhanced by the surface plasmon resonance effect from the Au nanoparticles.

© 2016 Elsevier B.V. All rights reserved.

## 1. Introduction

The rapid expansion of global industry has led to serious environmental problems such as water and air pollution, which present health problems to mankind [1]. In recent years, a number of technologies (such as biological, thermal, chemical, etc.) have been developed for the removal of toxic organic compounds from industrial wastewater [2–4]. Among them, photocatalysis is one of green technologies that allows the utilization of solar light for organic pollutants degradation, hence providing a potential route for cleaning up the environment [5,6]. Phenol and bisphenol A (BPA) are the most abundant organic contaminants in industrial wastewater [7,8]. They are toxic at rather low concentrations and relatively stable against biodegradation. Therefore, finding effective methods to

remove phenol and BPA from wastewater has become an important issue for environmental science.

The Aurivillius phase of  $\text{Bi}_4\text{Ti}_3\text{O}_{12}$  (BTO) has received much attention for its photocatalytic activity in degrading organic pollutants and water splitting [9–12]. The structure of  $\text{Bi}_4\text{Ti}_3\text{O}_{12}$ , i.e.,  $(\text{Bi}_2\text{O}_2)^{2+}(\text{Bi}_2\text{Ti}_3\text{O}_{10})^{2-}$ , is achieved by alternative stacking of a triple layer of  $\text{TiO}_6$  octahedral and a monolayer of  $(\text{Bi}_2\text{O}_2)^{2+}$  along the  $c$  axis.  $(\text{Bi}_2\text{O}_2)^{2+}$  and  $(\text{Bi}_2\text{Ti}_3\text{O}_{10})^{2-}$  layers form an inner electric field, which promotes the separation of photo-generated electrons and holes giving rise to an enhanced photocatalytic activity [10,13]. However, pure  $\text{Bi}_4\text{Ti}_3\text{O}_{12}$  is not very efficient for photocatalysts due to its large band gap ( $E_g = 2.95$  eV) and high recombination rate of photo-generated electron-hole pairs [14]. Much effort has been devoted to the modification of  $\text{Bi}_4\text{Ti}_3\text{O}_{12}$  with a view to increasing its photocatalytic activity during recent years [15,16]. There is evidence that metal-doping is an effective method for enhancing visible light response and reducing the recombination rate of photo-induced electron-hole pairs [17–20]. Many experimental results show that metal-doped  $\text{Bi}_4\text{Ti}_3\text{O}_{12}$  has higher photocatalytic activity than pure  $\text{Bi}_4\text{Ti}_3\text{O}_{12}$ , for instance, La-doped  $\text{Bi}_4\text{Ti}_3\text{O}_{12}$  [21],

\* Corresponding author at: School of Physics and Information Technology, Shaanxi Normal University, Xi'an 710062, China.

\*\* Corresponding authors.

E-mail addresses: zgq2006@snnu.edu.cn (G. Zhu), zhurl@gig.ac.cn (R. Zhu).

Cr-doped  $\text{Bi}_4\text{Ti}_3\text{O}_{12}$  [22], Zn-doped  $\text{Bi}_4\text{Ti}_3\text{O}_{12}$  [23], and Nd-doped  $\text{Bi}_4\text{Ti}_3\text{O}_{12}$  [24].

Among the transition metal ions,  $\text{Fe}^{3+}$  ions can form a dopant energy-band and reduce the band gap of the photocatalysts, hence electrons can be excited by photons of lower energy. More importantly,  $\text{Fe}^{3+}$  can turn into  $\text{Fe}^{2+}$  or  $\text{Fe}^{4+}$  ions by trapping photo-generated electrons or holes, respectively, which can hinder the recombination process and enhance the photocatalytic activity [25]. In addition, the radius of  $\text{Fe}^{3+}$  (0.79 Å) is similar than that of  $\text{Ti}^{4+}$  (0.75 Å) [25], so  $\text{Fe}^{3+}$  ions can be easily accommodated into the crystal lattice of  $\text{Bi}_4\text{Ti}_3\text{O}_{12}$ . Therefore, it is expected that the photocatalytic activity of  $\text{Bi}_4\text{Ti}_3\text{O}_{12}$  for removing organic pollutants can be improved by  $\text{Fe}^{3+}$ -doping. The effect of  $\text{Fe}^{3+}$ -doping on photocatalytic reactivity has been studied and reported in a number of previous publications, for instance,  $\text{Fe}^{3+}$ -doped  $\text{BiOCl}$  [26],  $\text{Fe}^{3+}$ -doped  $\text{Bi}_2\text{O}_3$  [27],  $\text{Fe}^{3+}$ -doped  $\text{Bi}_2\text{WO}_6$  [28], and  $\text{Fe}^{3+}$ -doped  $\text{BiVO}_4$  [29].

By considering a much related topic, highly dispersed noble metal nanoparticles (Au, Ag, Cu, etc) loaded on the surface of semiconductor materials exhibit extraordinary high activity for photocatalytic degradation of organic contaminants [30–33]. There are plenty of experimental results reporting the effectiveness of this method involving model catalysts such as  $\text{Au}/\text{TiO}_2$  [34],  $\text{Ag}/\text{Bi}_2\text{O}_3$  [35],  $\text{Ag}/\text{C}_3\text{N}_4$  [36],  $\text{Ag}/\text{BiVO}_4$  [37],  $\text{Ag}/\text{Bi}_2\text{WO}_6$  [38], and  $\text{Ag}/\text{BiPO}_4$  [39]. The high activity is related to the retardation of electron-hole recombination due to the trapping of electrons. Moreover, noble metal nanoparticles has a wide range of absorption spectrum in the visible light region because of the surface plasmon resonance (SPR), which is defined as the collective oscillation of the conduction electrons [40–44]. As a result, photocatalytic activity is improved by the SPR effect of noble metal nanoparticles on the semiconductor surface.

In this work, Au nanoparticles loaded on the Fe/BTO photocatalysts with exposed {001} facets were synthesized by molten salt method and low-temperature hydrogen peroxide reduction method. Phenol and bisphenol A were chosen as model organic pollutants to evaluate the photocatalytic activity of Fe/BTO and Au-2%Fe/BTO photocatalysts. Compared with pure BTO, the as-prepared Au-2%Fe/BTO composites photocatalysts displayed a much higher photocatalytic activity for photo-degradation of phenol and bisphenol A under light irradiation. Furthermore, a comprehensive photocatalytic mechanism of Au-Fe/BTO composites was also proposed and discussed in detail.

## 2. Experimental

### 2.1. Sample preparation

All the chemical reagents were analytical grade and used without further purification. All the  $\text{Fe}^{3+}$ -doped  $\text{Bi}_4\text{Ti}_3\text{O}_{12}$  samples were prepared by a one-step molten salt synthesis method. A typical procedure for preparing  $\text{Fe}^{3+}$ -doped  $\text{Bi}_4\text{Ti}_3\text{O}_{12}$  sample is described in the following: First, the powders of  $\alpha\text{-Bi}_2\text{O}_3$ , P25, and  $\text{Fe}_2\text{O}_3$  were mixed according to the composition of  $\text{Bi}_4\text{Fe}_x\text{Ti}_{3-x}\text{O}_{12}$ , with NaCl and KCl the co-solvents at a molar ratio of NaCl: KCl:  $\text{Bi}_4\text{Fe}_x\text{Ti}_{3-x}\text{O}_{12}$  = 60: 60: 1. Secondly, the above mixture was ground thoroughly for over 15 min with an agate mortar and pestle. The resulting mixture was then heated at 750 °C for 2 h in air. The obtained product was washed in an ultrasonic bath with deionized water for 6 times, before washing twice with ethanol. Finally, the as-prepared powders were dried at 80 °C. The  $\text{Bi}_4\text{Fe}_x\text{Ti}_{3-x}\text{O}_{12}$  samples were achieved by adjusting the “x” to 0, 0.02, 0.04, and 0.06. After that, the as-prepared samples were denoted as BTO, 2%Fe/BTO, 4%Fe/BTO, and 6%Fe/BTO, respectively. For the preparation of Au-2%Fe/BTO sample, 0.5 g of 2%Fe/BTO sample was dispersed in 100 mL glass beaker with 20 mL deionized water, then 2 mL  $\text{HAuCl}_4$  (0.01 mol/L) and 20 mL  $\text{H}_2\text{O}_2$  (0.1 mol/L) were added into the 2%Fe/BTO dispersion under continuously stirring. After stirring for 2 h, the obtained precipitates were washed with deionized water and ethanol for several times, and then dried at 80 °C.

### 2.2. Characterization

The crystalline phases were determined using X-ray powder diffraction (XRD) at room temperature with  $\text{Cu K}\alpha$  radiation on a Bruker D8 Advance instrument in  $2\theta$  range of 10–80°. The scanning electron microscopy (SEM) images were recorded by a field emission scanning electron microscopy (Nova NanoSEM 450, FEI). The transmission electron microscopic (TEM) images of the samples were acquired using a JEM-2100 electron microscope (JEOL, Japan). The chemical states of elements in the samples were determined by X-ray photoelectron spectroscopy (XPS) using a VG ESCALAB MKII X-ray photoelectron spectrometer (VG Scienta, USA) with Mg Ka radiation. Photoluminescence (PL) spectra of the as-prepared samples was observed with a He-Cd laser (325 nm) as the excitation source at room temperature. The UV-vis adsorption spectra of the samples was measured on a Perkin-Elmer Lambda 950 UV-VIS-NIR spectrophotometer.

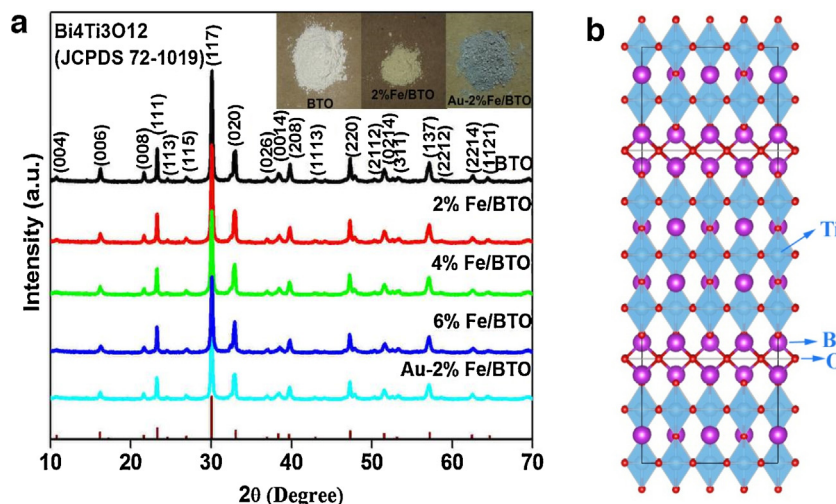


**Fig. 1.** (a) XRD patterns of pure BTO, 2%Fe/BTO, 4%Fe/BTO, 6%Fe/BTO and Au-2%Fe/BTO samples; (b) crystal structure of orthorhombic BTO.

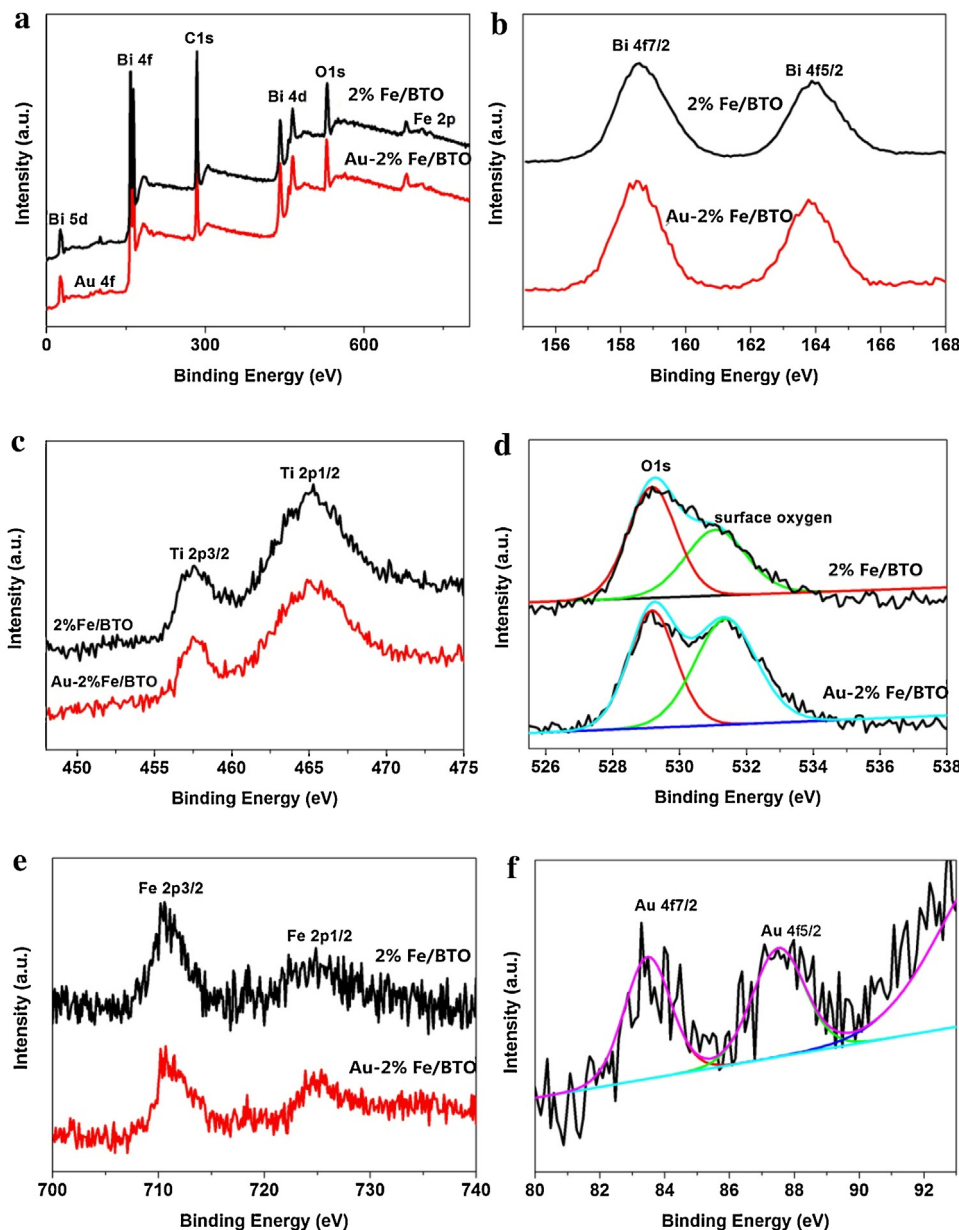


**Fig. 2.** (a) Survey XPS spectrum of the 2%Fe/BTO and Au-2%Fe/BTO samples; The high-resolution XPS spectra of (b) Bi 4f, (c) Ti 2p, (d) O 1s, (e) Fe 2p, and (f) Au 4f.

### 2.3. Photocatalytic test

Phenol and bisphenol A (BPA) were used as probe organic pollutants, and a 400 W halogen lamp was employed as a visible light source. The photo-degradation reaction temperature was maintained at 25 °C by the circulation of water. Prior to irradiation, the as-prepared samples as photocatalyst for phenol and BPA were continuously stirred in the dark for 30 min to ensure an adsorption-desorption equilibrium. During the irradiation, 2 mL of suspension was taken out at a given interval for subsequent pollutant concentration analysis by using a U-3010 UV-vis spectrophotometer. The wavelength of phenol and BPA was detection at 270 nm and 277 nm, respectively. Total organic carbon (TOC) concentration was measured by automatic total organic carbon analyzer (VARIO, Elementar, Germany).

## 3. Results and discussion

### 3.1. XRD analysis

**Fig. 1a** shows the XRD patterns of all the as-synthesized samples. All the diffraction peaks in **Fig. 1a** can be indexed according to the standard data of orthorhombic BTO with the space group *Aba*2 (JCPDS 72-1019). The Orthorhombic BTO is described with a general formula of  $(\text{Bi}_2\text{O}_2)^{2+}(\text{Bi}_2\text{Ti}_3\text{O}_{10})^{2-}$ , which is constructed by alternative stacking with a triple layer  $\text{TiO}_6$  octahedral and a monolayer of  $(\text{Bi}_2\text{O}_2)^{2+}$ , as shown in **Fig. 1b**. The  $\text{BiOCl}$ ,  $\text{Fe}_2\text{O}_3$  or  $\text{FeTiO}_3$  phases were not detected in the XRD patterns of all the Fe/BTO samples (**Fig. 1a**). In addition, the diffraction peaks of the cubic Au phase are also absent in the XRD patterns of Au-2%Fe/BTO. This may attribute to the low concentration of gold in the composite sample. Although,

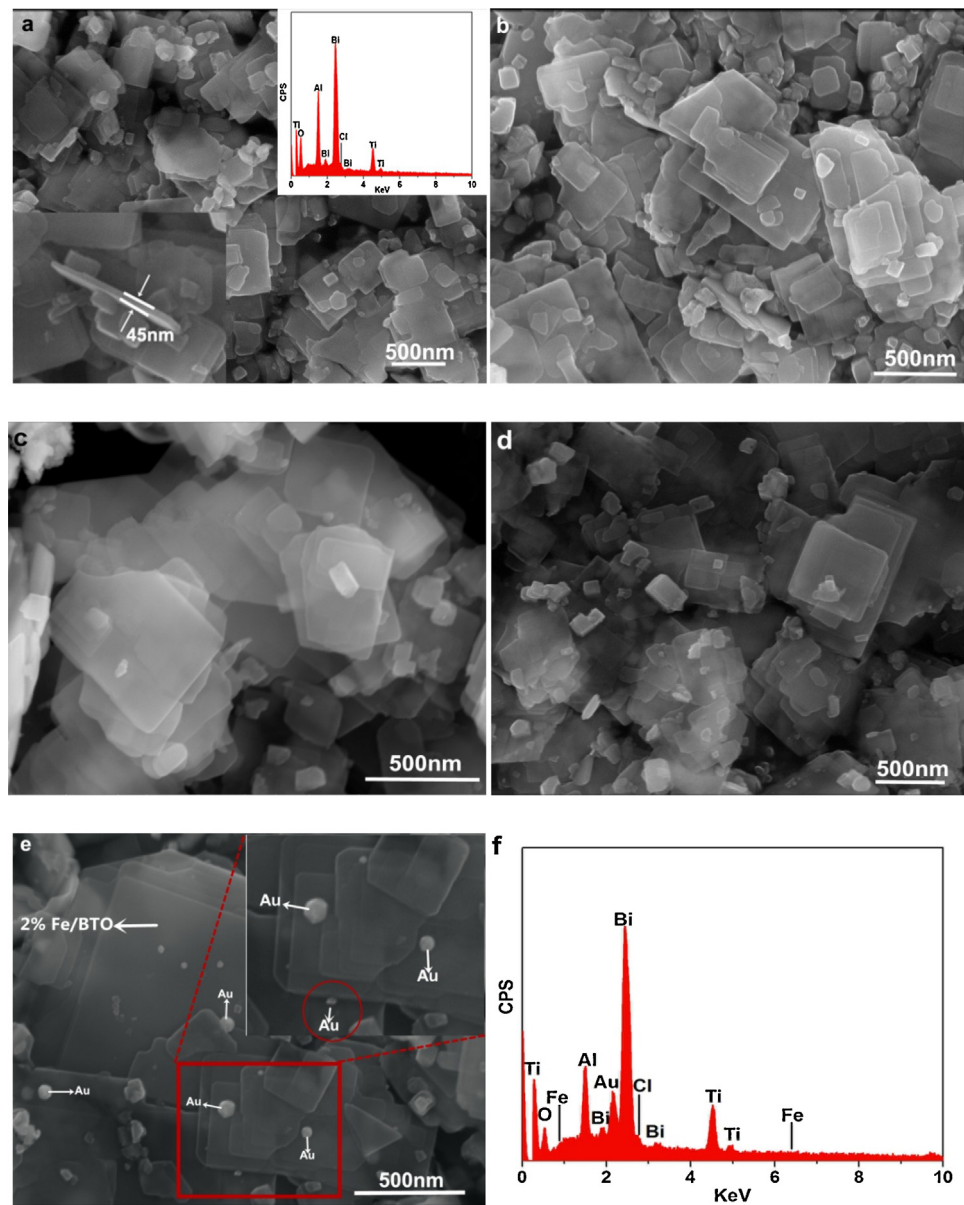


**Fig. 3.** (a) SEM images of BTO and the inset spectrum shows the corresponding EDS patterns; SEM images of (b) 2%Fe/BTO, (c) 4%Fe/BTO, (d) 6%Fe/BTO and (e) Au-2%Fe/BTO; (f) EDS patterns of Au-2%Fe/BTO sample.

The XRD patterns did not provide evidence for the presence of Au in the Au-2%Fe/BTO composite powders. However, the color of Au-2%Fe/BTO composite photocatalysts became gray (inset in Fig. 1a) after modified with Au particles. Apparently, it can be deduced that Au has been incorporated into the samples.

### 3.2. XPS analysis

To investigate the chemical state of elements and the surface defects, X-ray photoelectron spectroscopy (XPS) analysis was carried out on the 2%Fe/BTO and Au-2%Fe/BTO samples and the results are shown in Fig. 2. The obtained binding energies in XPS analysis were corrected by specimen charging which was executed by referencing the C1 s line to 284.6 eV. The survey XPS spectrum in Fig. 2a clearly reveals that the Au-2%Fe/BTO sample mainly consists of Bi, Ti, O, Fe and Au. XPS signals of Bi 4f (Fig. 2b) were observed at binding energies around 164.3 eV (Bi 4f<sub>5/2</sub>) and 158.8 eV (Bi 4f<sub>7/2</sub>), which are perfectly consistent with the data of Bi<sub>2</sub>O<sub>3</sub> powders [45]. The XPS signals in Fig. 2c are related to Ti 2p, which were observed

at binding energies at around 465.1 eV (Ti 2p<sub>1/2</sub>) and 457.8 eV (Ti 2p<sub>3/2</sub>). This is in agreement with that of pure TiO<sub>2</sub> [46]. In Fig. 2d, it can be seen that the O 1s peak is deconvoluted into two symmetric Gaussian curves at peak positions around 529.6 and 531.2 eV. These two peaks are assigned to oxygen in the prepared sample lattice [47] and surface-adsorbed oxygen, respectively. Consequently, the peaks around 710 and 724 eV (Fig. 2e) are related to the binding energies of Fe 2p<sub>3/2</sub> and Fe 2p<sub>1/2</sub> for the ferric (III) ion [48]. In Fig. 2f, doublet peaks are observed at 82.8 and 86.6 eV, which are from the Au 4f<sub>7/2</sub> and Au 4f<sub>5/2</sub> levels. The observation of the Au 4f peaks prove that Au exists as Au<sup>0</sup> in Au-2%Fe/BTO sample [49]. From the above results, it is concluded that the Fe<sup>3+</sup> ions and Au nanoparticles were successfully incorporated into the BTO sample.

### 3.3. SEM analysis

The morphologies of the as-prepared pure BTO, Fe/BTO, and Au-2%Fe/BTO are shown in Fig. 3. As shown in Fig. 3a, the as-prepared BTO sample consists of uniform sheet-like sub-microstructures,

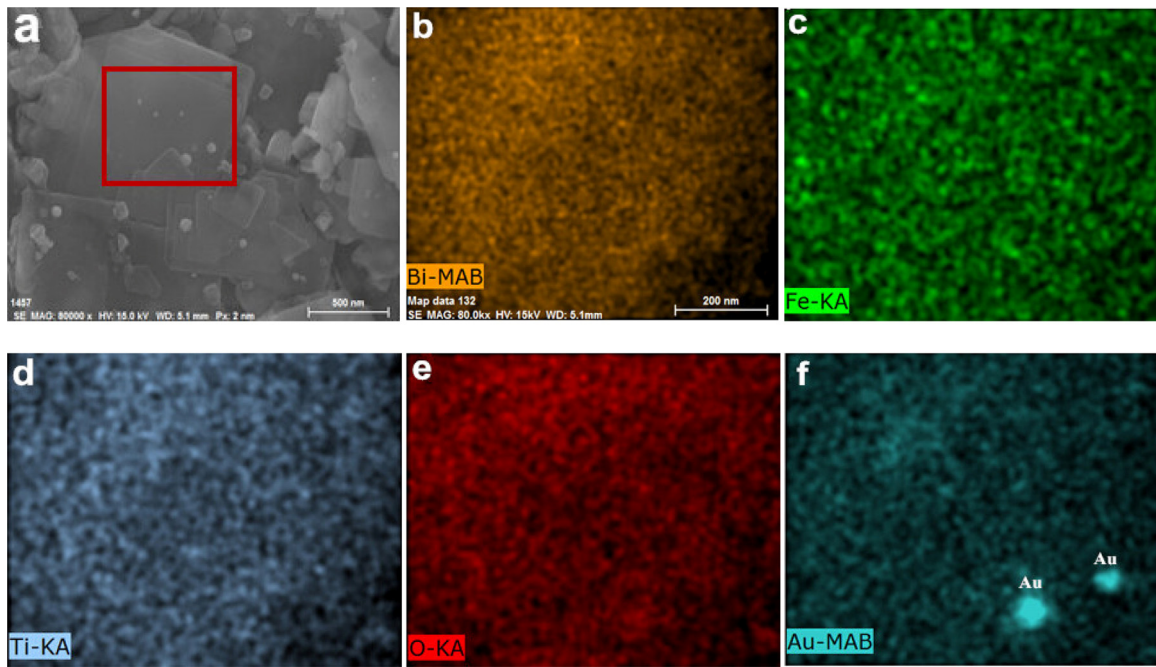


**Fig. 4.** (a) SEM image for Au-2%Fe/BTO sample; (b)–(f) EDS mapping images of the Bi, Fe, Ti, O, Au elements respectively.

with a thickness of ~45 nm and the average side length of the sheets is ~500–1000 nm. The inset spectrum in Fig. 3a is the EDS spectrum of the sheet-like sub-microstructure, which shows the Bi/Ti ratios is 1.33:1. This is close to ratio from the stoichiometric BTO. The signal of aluminum is detected due to the aluminum sample stage. The detection of Cl is due to residuals in the synthesized samples. It can be seen from the SEM images in Fig. 3b–d that there are no significant changes on morphology after  $\text{Fe}^{3+}$ -doping. Fig. 3e shows the SEM image of Au-2%Fe/BTO sample. The nanoparticles with diameter around 20–50 nm could be attributed to the dispersed Au nanoparticles on the surface of the nanosheets. It can see clearly that most of these Au nanoparticles are loaded on the surface of the nanosheets, but there are also some Au nanoparticles loaded on the side of the nanosheet (the circle inset in Fig. 3e). The EDS pattern in Fig. 3f shows that there are Bi, Ti, Fe, Au and Cl elements in the Au-2%Fe/BTO sample. The Fe/Bi ratio is 0.97:200, which is close to the theoretical value of 1/200. The EDS Mapping was selected for further analysis of elemental distribution on the Au-2%Fe/BTO sample. As shown in Fig. 4b–e, the Bi, Fe, Ti, O elements were well distributed in the region. Fig. 4f shows the elemental distribution of Au in the square area in Fig. 4a, which gives a very clear signal of the presence of Au nanoparticles. From the above results of XRD, XPS, SEM, EDS and EDS mapping, it can be concluded that the  $\text{Fe}^{3+}$  ions are well doped into the BTO lattice and Au nanoparticles are located on the surface of the BTO nanosheets.

#### 3.4. TEM and HRTEM analysis

The microstructures and morphological details of the 2%Fe/BTO and Au-2%Fe/BTO samples were further observed by TEM and HRTEM. According to Fig. 5a, the 2%Fe/BTO sample has a sheet structure, which is consistent with the SEM results shown in Fig. 3b. Fig. 5b shows the HRTEM image of a single 2%Fe/BTO sheet that the lattice fringes are spacing with:  $d = 0.270 \text{ nm}$  and  $d = 0.272 \text{ nm}$ . This is ascribed to the (020) and (200) crystallographic planes of BTO respectively, and implies the exposed facets of sheet-like 2%Fe/BTO nanostructures as {001} facets [12]. The inset image in Fig. 5b is SAED, which indicates that the as-prepared sheet-like 2%Fe/BTO nanostructures has a single crystal characteristic. Fig. 5c shows the

TEM image of the Au-2%Fe/BTO sample, it can see clearly that some of the nanoparticles are present with an average diameter around 20–50 nm and located on the sheets surface. From the HRTEM image in Fig. 5d, the nanoparticles can be seen to sit on the surface of the sheet. The spacing of the lattice is  $d = 0.272 \text{ nm}$ , which is ascribed to the (200) crystallographic plane of BTO, whereas the lattice fringes with the spacing of  $d = 0.240 \text{ nm}$  match the (111) crystallographic planes of Au nanoparticles. From the TEM and HRTEM results in Fig. 5, we confirm that most of the Au nanoparticles were deposited on the flat surfaces of the 2%Fe/BTO nanosheets with exposed {001} facets. However, there is also some possibility that some Au nanoparticles are attached to the sides of the Fe/BTO nanosheet with exposed {001} facets, as evidenced from TEM and HRTEM images in Fig. 5e–h. From the above results, it is concluded that the  $\text{Fe}^{3+}$  ions were successfully incorporated into the BTO lattice and Au nanoparticles are mostly located on the surface of the BTO sheets, consistent with the XRD, XPS, SEM, and EDS mapping results.

#### 3.5. UV-vis DRS analysis

Fig. 6 shows the UV-vis diffuse reflectance spectra of BTO, Fe/BTO and Au-2%Fe/BTO samples. It can see clearly that the BTO exhibits an optical response at wavelengths shorter than 450 nm. This indicates that the BTO sample is active under UV light and a narrow region of the visible light. The light absorption edge in the UV-vis diffuse reflectance spectrum of Fe/BTO was extended to the visible light region (450–600 nm) after  $\text{Fe}^{3+}$ -doping. More importantly, the Au-2%Fe/BTO shows a slight red shift in the absorption edge, and a significant enhancement of visible light absorption can be noted at 420–800 nm. Another absorption band at about 500 nm can be seen in the UV-vis spectra of Au-2%Fe/BTO. The similar effect has been reported and the reason of this feature is attributed to the surface plasmon absorption of spatially confined electrons in Au nanoparticles [50,51], and the optical absorption near the band edge follows the Tauc equation:

$$\alpha h\nu = A(h\nu - E_g)^n/2 \quad (1)$$

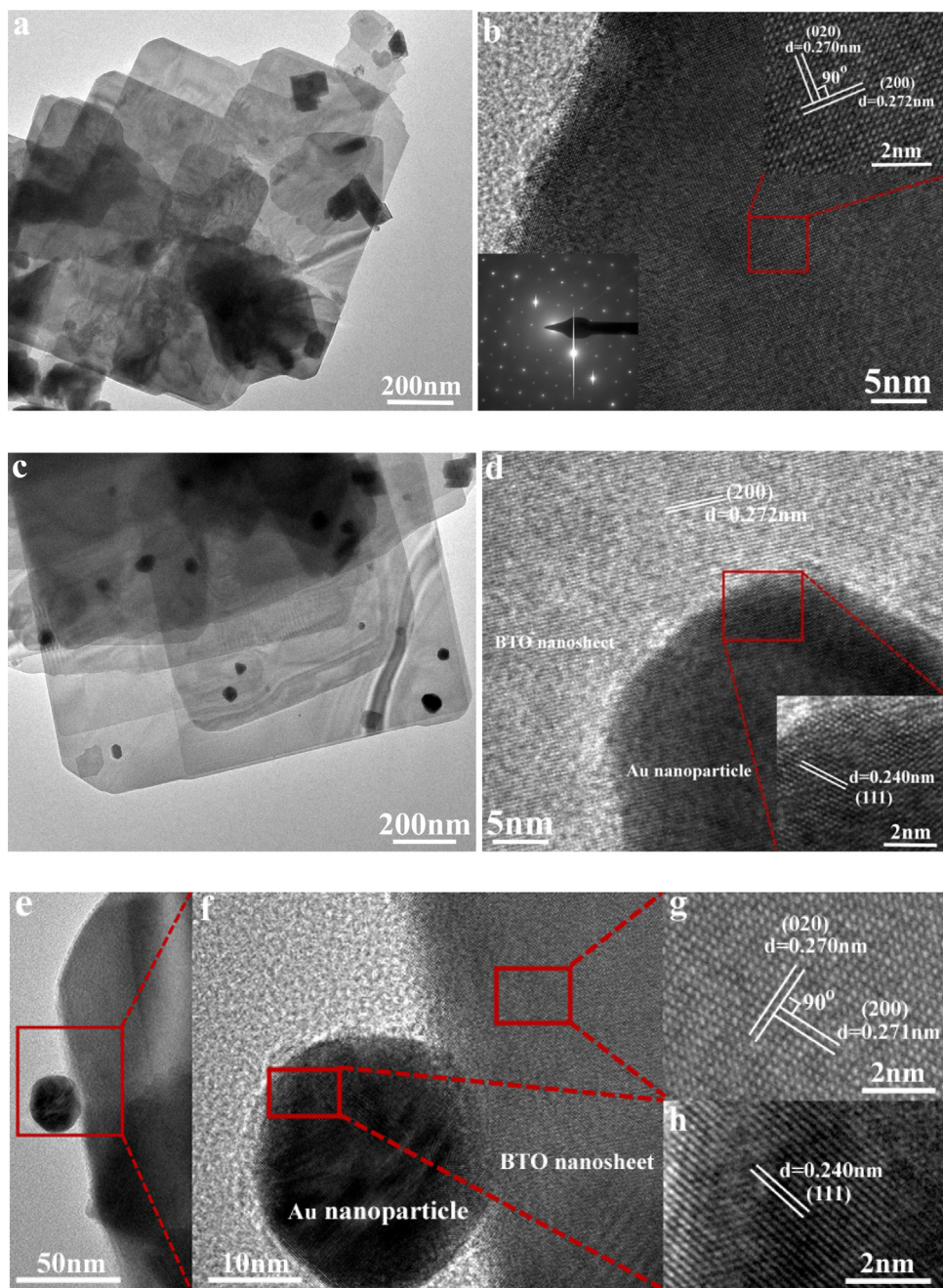


**Fig. 5.** (a) TEM and (b) HRTEM images of 2% Fe/BTO; (c,e) TEM and (d,f-h) HRTEM images of Au-2%Fe/BTO (c-h) samples.

where A is constant,  $\alpha$ ,  $h$ ,  $\nu$ , and  $E_g$ , are the absorption coefficient, Planck's constant, light frequency, and band gap, respectively. The power index n depends on the type of electronic transition, n equals to 1 for a direct band-gap material and 4 for an indirect band-gap material. For semiconductors, the square of absorption coefficient is usually linearly proportional to the energy ( $h\nu$ ) in the absorption edge region during the direct optical transition process. The plots of  $(\alpha h\nu)^{1/2}$  versus energy ( $h\nu$ ) is shown in Fig. 6 (inset). The  $E_g$  values of pure BTO, 2%Fe/BTO, 4%Fe/BTO and 6%Fe/BTO samples can be calculated to be 2.92, 2.43, 2.36, and 2.28 eV, respectively.

### 3.6. Photo-degradation of bisphenol A and phenol

The photocatalytic activities of pure BTO and Fe/BTO samples were investigated by the degradation of BPA under visible light

irradiation. Temporal changes in the concentration of BPA were monitored by examining the variation in maximal absorption in the UV-vis spectra at 277 nm. Fig. 7a shows the variation of BPA concentration ( $C/C_0$ ) over BTO, 2%Fe/BTO, 4%Fe/BTO, and 6%Fe/BTO photocatalysts against reaction time under light irradiation. To provide a point of reference, experiments were also performed on directly photolysis of BPA (a blank experiment) in the absence of photocatalysts. As a result, no obvious change in the BPA concentration within 60 min light irradiation was observed. Meanwhile, the photodegradation of BPA over BTO sample is around 75% after 60 min light irradiation, which indicates that the pure sheet-like BTO powders with photocatalytic is activated for the degradation of BPA under light irradiation. Moreover, under the same experimental conditions, the percentage of photodegraded BPA over 2%Fe/BTO, 4%Fe/BTO and 6%Fe/BTO photocatalysts has reached

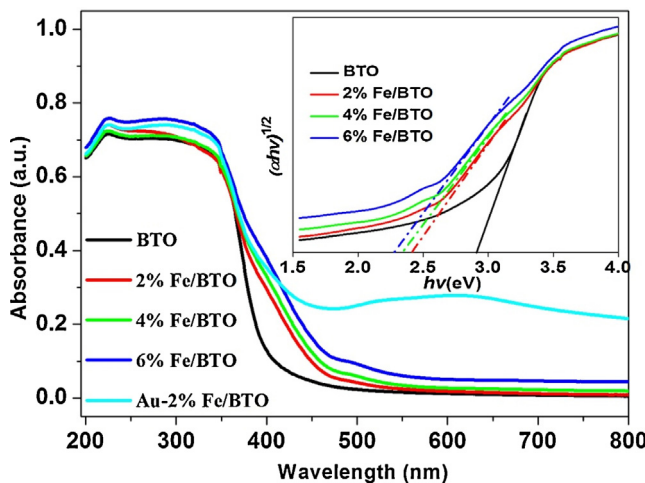


**Fig. 6.** UV-vis adsorption spectra of the pure BTO, Fe/BTO and Au-2%Fe/BTO samples and inset the plots of  $(\alpha h\nu)^{1/2}$  versus energy ( $h\nu$ ).

89.6%, 84.2% and 79.8%, respectively. The above results indicate that the 2%Fe/BTO sample exhibits the highest photocatalytic activity. Furthermore, Phenol was also chosen for further examination of the photocatalytic activity with the pure BTO and Fe/BTO photocatalysts. Temporal changing for the concentration of phenol was monitored by examining the variation in maximal absorption in the UV-vis spectra at 270 nm. Fig. 7c shows the variation of phenol concentration ( $C/C_0$ ) over pure BTO and Fe/BTO photocatalysts against different durations of light irradiation. Under light irradiation, 2%Fe/BTO photocatalysts (Fig. 7c) also show the best photocatalytic activity for the degradation of phenol compared to pure BTO powders and other Fe/BTO photocatalysts. The total

photodegradation of phenol over BTO, 2%Fe/BTO, 4%Fe/BTO, and 6%Fe/BTO photocatalysts is 37.0%, 54.1%, 41.1%, and 28.8%, respectively.

According to the Langmuir–Hinshelwood (L–H) kinetics model [5], the photocatalytic process of BPA and phenol can be expressed as the following apparent pseudo-first-order kinetics equation:

$$\ln(C_1/C) = kt \quad (2)$$

where  $C_1$  is the concentration of organic pollutant after the establishment of an absorption-desorption equilibrium ( $t=0$ ) and  $C$  is the concentration of organic pollutant at time  $t$  (inset in Fig. 7b and d). According to Fig. 7b and d, the  $k$  of BTO, 2%Fe/BTO, 4%Fe/BTO, and 6%Fe/BTO was calculated as: 0.0214, 0.0349, 0.0296, and 0.0260 min<sup>-1</sup> for BPA in (Fig. 7b), and 0.0047, 0.0081, 0.0056, and 0.004 min<sup>-1</sup> for phenol in (Fig. 7d), respectively. The results in Fig. 7 show that the 2%Fe/BTO sample has the highest activity for breaking down BPA and phenol.

Under identical experimental conditions, the effect of adding Au nanoparticles to the Au-2%Fe/BTO composite photocatalysts was studied. Fig. 8 shows the variation of BPA and phenol concentrations ( $C/C_0$ ) over pure BTO, 2%Fe/BTO, and Au-2%Fe/BTO photocatalysts as a function of reaction time under light irradiation. Fig. 8a shows the percentage of photodegraded BPA over pure BTO, 2%Fe/BTO, and Au-2%Fe/BTO photocatalysts reaches 72.3%, 87.6%, and 99.2%, after 50 min light irradiation. It can be seen clearly that compared with pure BTO and 2%Fe/BTO, the degradation efficiency of BPA by Au-2%Fe/BTO has been improved by 26.9% and 11.6%, respectively. After 80 min light irradiation, the percentages of photodegraded phenol (Fig. 8c) over BTO, 2%Fe/BTO, and Au-2%Fe/BTO photocatalysts are 37.0%, 54.1%, and 64.3%, respectively. Fig. 8 (b) and (d) give the  $k$  values of BPA and phenol over BTO, 2%Fe/BTO, and Au-2%Fe/BTO, which are 0.0214, 0.0349, and 0.0789 min<sup>-1</sup> for BPA; 0.0047, 0.0081, and 0.0096 min<sup>-1</sup> for phenol. From the above

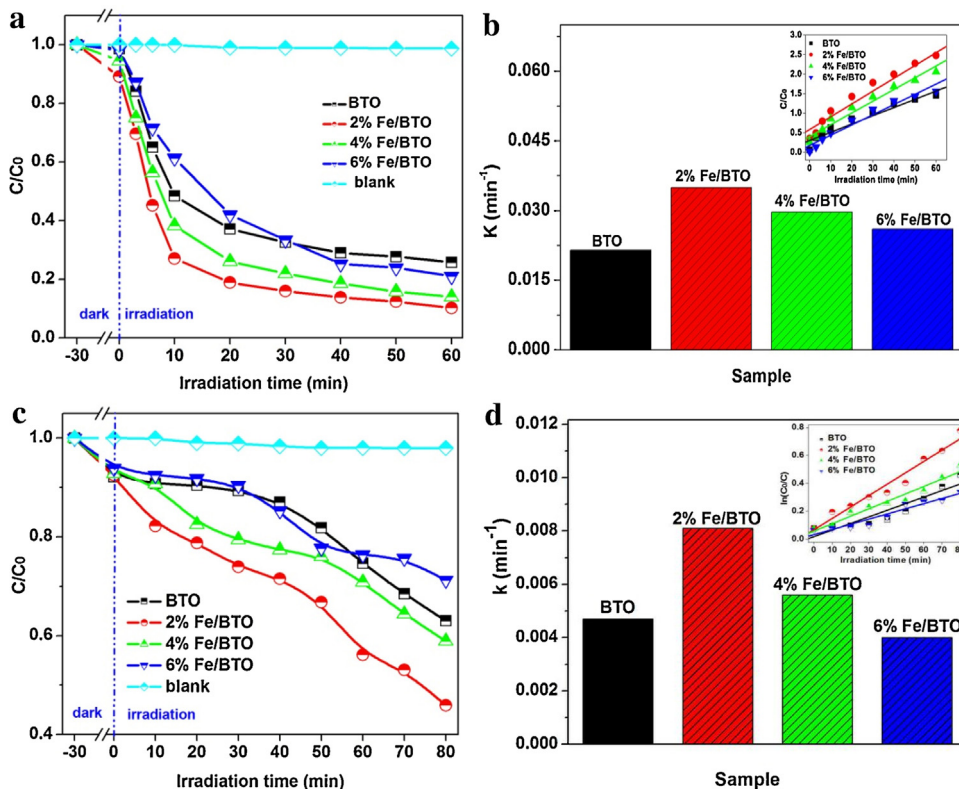


**Fig. 7.** (a) and (c) are the variation of bisphenol A and phenol; (b) and (d) are the concentration ( $C/C_0$ ) over BTO, 2%Fe/BTO, 4%Fe/BTO and 6%Fe/BTO photocatalysts samples with time under light irradiation and the pseudo-first-order kinetics for bisphenol A and phenol.

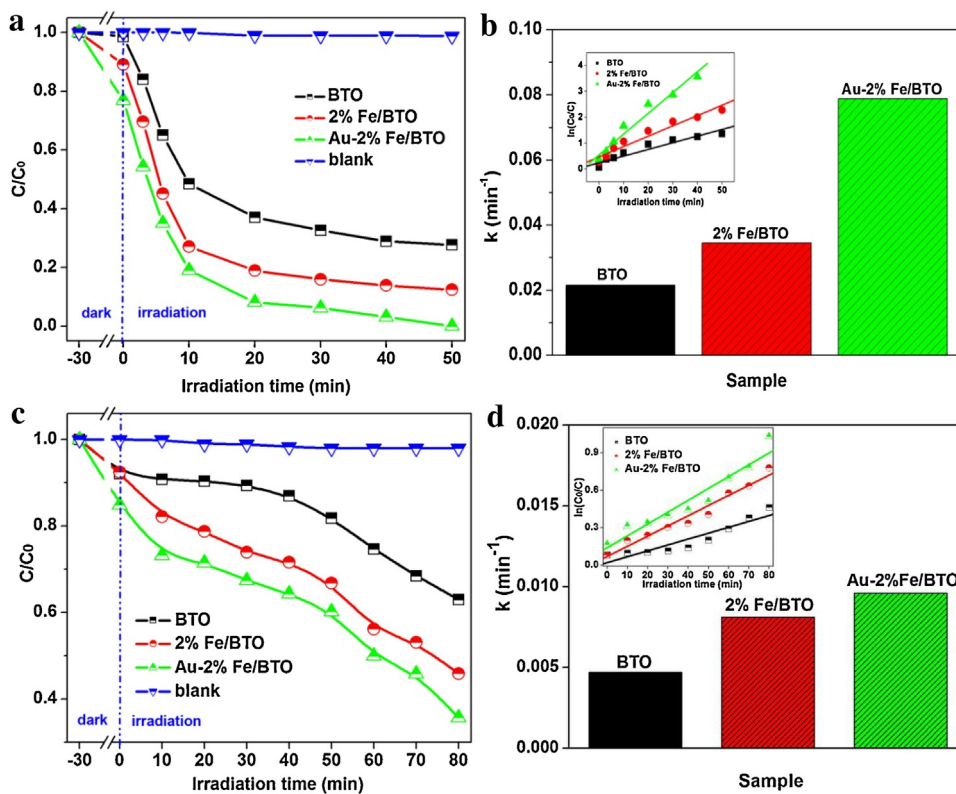


**Fig. 8.** (a) and (b) are the photocatalytic activity for degradation of BPA with different sample of BTO, 2%Fe/BTO and Au-2%Fe/BTO under light irradiation.; (c) and (d) are the photocatalytic activity for degradation of phenol with different sample of BTO, 2%Fe/BTO and Au-2%Fe/BTO under light irradiation.

results in Fig. 8, the Au-2%Fe/BTO sample can present a higher degradation rate for BPA and phenol in comparison with pure BTO and 2%Fe/BTO. The Au metal nanoparticles have a great effect on the photocatalytic activity for the composite of Au-2%Fe/BTO. According to previously reported data, the photocatalytic enhancement property was described with an enhancement factor “ $E_f$ ” when the metal particle was loaded on the semiconductor [52]. Therefore, the enhancement factor  $E_f$  was also evaluated in our analysis and the values of 2.0 for phenol and 3.7 for BPA. The kinetics study of the phenol and BPA degradation over BTO, 2%Fe/BTO, and Au-2%Fe/BTO under visible light irradiation are generally evidence the synergism of  $\text{Fe}^{3+}$ -doping and Au nanoparticles loading in the Au-2%Fe/BTO, especially the photocatalytic degradation for BPA. From the above results, it can also be seen that photodegradation of BPA occurs at a faster rate than that for phenol. This behavior is similar to that reported in previous works that some semiconducting photocatalysts have different selective photocatalytic properties for different types pollutants [53,54].

The removal of total organic carbon (TOC) was chosen as a mineralization index to characterize the phenol and BPA degradation. Under light irradiation, the time independence TOC data of phenol and BPA solution is measured with Au-2%Fe/BTO catalyst in Fig. 9. It is observed that 95.7% of the TOC was eliminated for BPA after 50 min of light irradiation and 59.2% of the TOC was eliminated for phenol after 80 min of light irradiation. These results indicate that most of the phenol and BPA were mineralized in the photocatalytic process, which is important for practical applications of Au-2%Fe/BTO photocatalysts to avoid secondary pollution.

### 3.7. Trapping experiment

It is well known, in the photocatalytic oxidation process of organic pollutants, there are series of photoinduced reactive

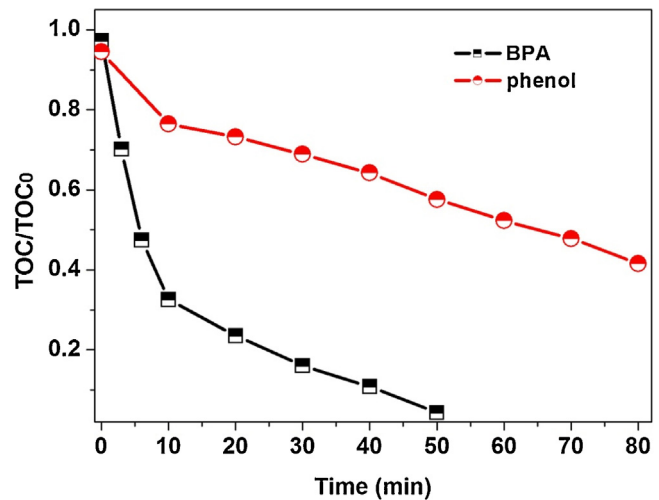


**Fig. 9.** TOC removal in the presence of Au-2%Fe/BTO photocatalysts for phenol and BPA under light irradiation.

species, including  $\cdot\text{OH}$ ,  $\cdot\text{O}_2^-$ , and  $\text{h}^+$ , which will be directly involved in the process after the electron-hole pairs are generated under light irradiation [55]. In order to evaluate the kind of reactive species, the quenchers of ammonium oxalate (AO), isopropyl alcohol (IPA) and benzoquinone (BQ) were used to scavenge the relevant reactive species during the photodegradation of BPA and phenol over Au-2%Fe/BTO photocatalysts under light irradiation. According to this work, the AO (1.0 mmol/L), IPA (1.0 mmol/L), and BQ (1.0 mmol/L) were adopted as hole ( $\text{h}^+$ ) and hydroxyl radicals ( $\cdot\text{OH}$ ) superoxide anions ( $\cdot\text{O}_2^-$ ) scavengers, respectively, and the corresponding results were shown in Fig. 10. Under the addition of AO and BQ, there is only about 15% and 35.3% of BPA in the

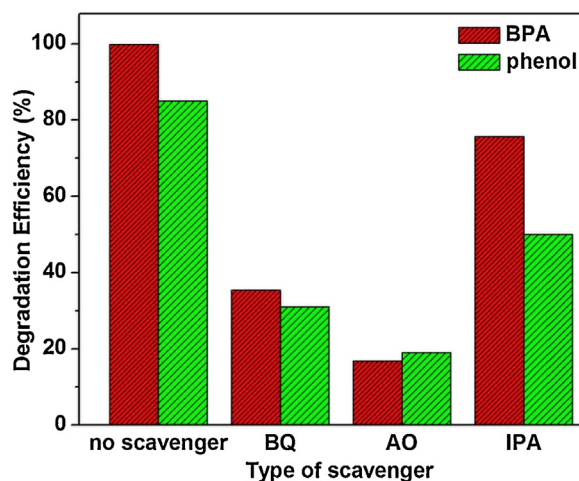


**Fig. 10.** Photocatalytic activity for degradation of BPA and phenol with different quenchers under light irradiation.

solution that was degraded under light irradiation, and 19% and 31.2% of phenol was degraded under the same condition. Overall, the above results can demonstrate that the photo-generated  $\text{h}^+$  and  $\cdot\text{O}_2^-$  species could play the dominant roles for the degradation of BPA or phenol over the Au-2%Fe/BTO photocatalysts under light irradiation and the photo-generated  $\text{h}^+$  plays more significant part than the  $\cdot\text{O}_2^-$  species.

### 3.8. PL spectra and I-V analysis

The separation rate of photoexcited electron-hole pairs is also an important factor for the photocatalytic activity of a photocatalyst. The transient photocurrent ( $I$ - $V$ ) and photoluminescence (PL) spectroscopic measurements are useful in demonstrating the photo-induced charge separation in photocatalysts [35,55]. The transient photocurrent responses for BTO, 2%Fe/BTO, and Au-2%Fe/BTO were also recorded under 300 W Xenon lamp irradiation through light-on and light-off cycles. In Fig. 11a, the Au-2%Fe/BTO photoelectrode shows 6.2 and 1.7 times higher photocurrent density compared with the BTO and 2%Fe/BTO photoelectrode, which indicates the more efficient photo-induced charge separation and faster charge transfer in the Au-2%Fe/BTO. Efficiency of photo-induced charge carrier trapping, transfer, and separation on the semiconductor surface or near-surface was further examined by photoluminescence spectrum [56], and the results are shown in Fig. 11b. The prepared samples show a broad peak in the range of 350–600 nm and the Au-2%Fe/BTO and 2%Fe/BTO samples show a lower PL intensity than BTO sample. What is more,  $\text{Fe}^{3+}$  will be oxidized to  $\text{Fe}^{4+}$  by holes [25,26], after it doped in the Fe/BTO photocatalyst. This leads to the separation of electron-hole pairs. With the Au nanoparticles on the surface of 2%Fe/BTO, the Schottky barrier is formed at the Au-Fe/BTO interface. Therefore, Au nanoparticles can easily capture the photo-excited electrons from Fe/BTO, resulting in a lower recombination rate of  $\text{e}^-/\text{h}^+$  pairs. The lower intensity PL spectra for the Au-2%Fe/BTO composite photocatalysts can exhibit lower recombination rate of photoelectron and holes pairs if we compare with BTO and 2%Fe/BTO samples and generate the higher photocatalytic activity.

### 3.9. Photocatalytic mechanism

From the demonstration above, Au-2%Fe/BTO shows high photocatalytic activity for photodegradation of BPA and phenol under light irradiation, and the possible mechanisms for the enhancement in photocatalytic activity of Au-2%Fe/BTO were shown in Fig. 12a.

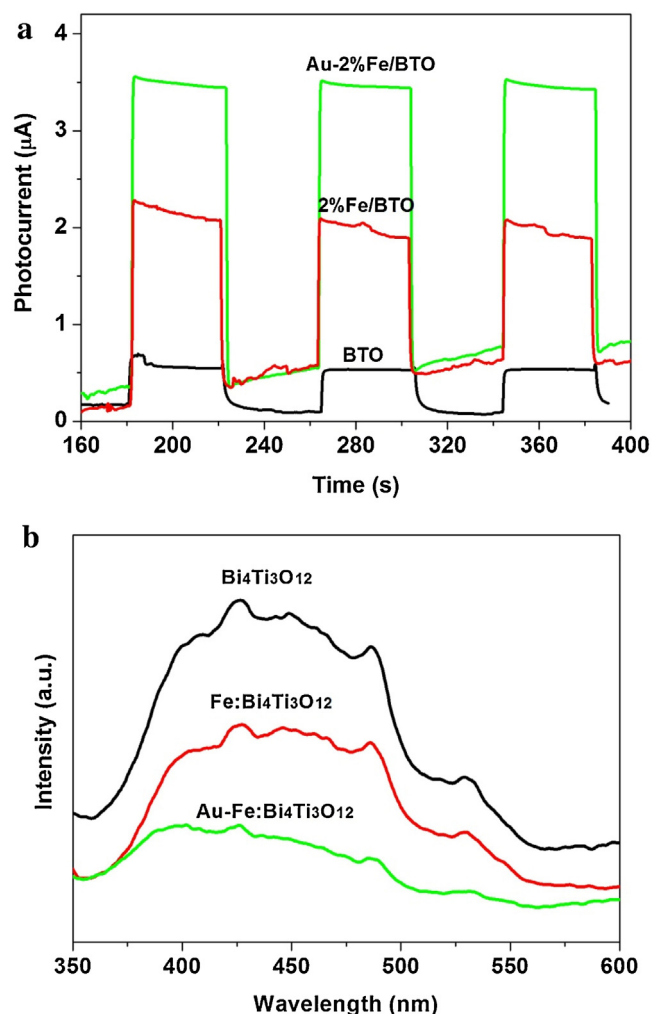


**Fig. 11.** Transient photocurrent (a) and photoluminescence spectra (b) of BTO, 2%Fe/BTO and Au-2%Fe/BTO samples.

Firstly, the results of HRTEM images in Fig. 5 show that 2%Fe/BTO nanosheets exposed {001} facets. The photoinduced electron-hole pairs are formed under light irradiation and then driven apart by the internal electric fields [12]. Therefore, the separation of photogenerated electron-hole pairs along [001] direction of Fe/BTO nanosheet can be promoted. On the other hand, the depolarisation fields can cause the separation of carriers, which will also suppress recombination rates, thereby increasing carrier lifetimes. Secondly, the photogenerated electrons and holes can be trapped by  $\text{Fe}^{3+}$ , which can turn into  $\text{Fe}^{2+}$  and  $\text{Fe}^{4+}$  ions by trapping photogenerated electrons and holes, respectively, hence, holding up the recombination process. However, the  $\text{Fe}^{2+}$  and  $\text{Fe}^{4+}$  ions have half-filled 3d<sup>5</sup> orbital and become relatively unstable than the  $\text{Fe}^{3+}$  ions. Therefore, the trapped charges can easily release from  $\text{Fe}^{2+}$  or  $\text{Fe}^{4+}$  ions and then migrate to the surface to initiate the photocatalytic reaction.  $\text{Fe}^{2+}$  ions can be oxidized to  $\text{Fe}^{3+}$  ions by transferring electrons to adsorbed  $\text{O}_2$  on the surface of BTO, and the adsorbed  $\text{O}_2$  is reduced to superoxide radical. This process can further degrade BPA and phenol. Similarly,  $\text{Fe}^{4+}$  ions are also reduced to  $\text{Fe}^{3+}$  ions by releasing electrons, while surface hydroxyl group can translate into hydroxyl radical. The trapped electrons can be further transferred to oxygen, which is adsorbed on the BTO surface hence generate superoxide radical. The trapped holes can also play a role in degradation of BPA and phenol. Thirdly, the loaded metal Au nanoparticles are remarkably enhance the absorption in the light

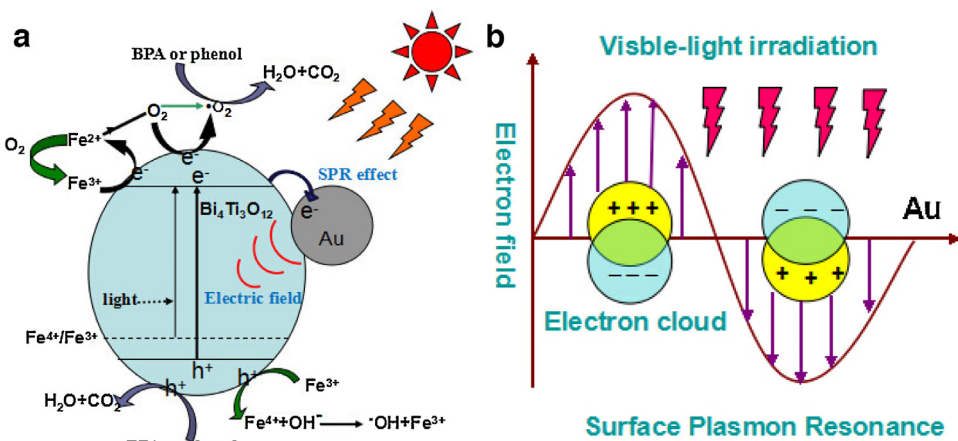
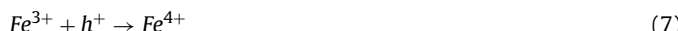
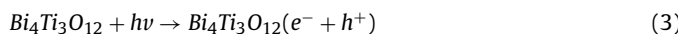


**Fig. 12.** (a) Schematic illustration of the charge separation and transfer in the Au-2%Fe/BTO composites under light irradiation; and (b) schematic for the surface plasmon resonance (SPR) effect of Au nanoparticles.

region. This is due to the surface plasmonic resonance effect (as shown in Fig. 12b), and create the plasmon induced electric field around Au. This promotes the formation rate of electrons and holes [57], and the Schottky barrier could enhance the interfacial electron transfer [58,59]. The detailed photo-degradation reaction processes are as follows:



## 4. Conclusions

A plasmonic Au-2%Fe/BTO composite photocatalysts was successfully prepared by a two-step chemical method. The SEM, TEM, and HRTEM observations revealed that the 2%Fe<sup>3+</sup>-doped BTO samples are composed of nanosheets with exposed {001} facets. The Au-2%Fe/BTO composite photocatalysts exhibited a higher photocatalytic activity for the photodegradation of phenol and bisphenol A than pure BTO sample. This is due to a combined effect of its special morphology, Fe<sup>3+</sup>-doping, and surface plasmon resonance of Au nanoparticles. The synthesized Au-2%Fe/BTO composite photocatalysts is thus of potential importance for some industrial wastewater treatment in the future.

## Acknowledgments

This work was supported by the National Natural Science Foundation of China (Grant nos. 51102160 and 51272148), the Fundamental Research Funds for the Central Universities (Grant nos. GK201401003, GK201602008 and GK201603013), and the research fund for Guangdong Provincial Key Laboratory of Mineral Physics and Materials (Grant no. GLMPM-017).

## References

- [1] R.S. Sonawane, M.K. Dongare, Sol-gel synthesis of Au/TiO<sub>2</sub> thin films for photocatalytic degradation of phenol in sunlight, *J. Mol. Catal. A: Chem.* 243 (2006) 68–76.
- [2] S. Baccella, G. Cerichelli, M. Chiarini, C. Ercole, Biological treatment of alkaline industrial waste waters, *Process Biochem.* 35 (2000) 595–602.
- [3] A.S. Sedlov, I.P. Ilyina, S.V. Sidorova, V.V. Shischenko, E.N. Potapkina, Small-waste technology of processing industrial waste water on the basis of thermal demineralization, *Desalination* 108 (1997) 361–364.
- [4] A.A. Markus, J.R. Parsons, E.W.M. Roex, P. de Voogt, R.W.P.M. Laane, Modeling aggregation and sedimentation of nanoparticles in the aquatic environment, *Sci. Total Environ.* 506–507 (2015) 323–329.
- [5] C.W. Tan, G.Q. Zhu, M. Hojaberdiev, K. Okada, J. Liang, X.C. Luo, P. Liu, Co<sub>3</sub>O<sub>4</sub> nanoparticles-loaded BiOCl nanoplates with the dominant {001} facets: efficient photodegradation of organic dyes under visible light, *Appl. Catal. B: Environ.* 152–153 (2014) 425–436.
- [6] J.G. Hou, C. Yang, Z. Wang, Q.H. Ji, Y.T. Li, G.C. Huang, S.Q. Jiao, H.M. Zhu, Three-dimensional Z-scheme AgCl/Ag/TaON heterostructural hollow spheres for enhanced visible-light photocatalytic performance, *Appl. Catal. B: Environ.* 142–143 (2013) 579–589.
- [7] C.Y. Wang, L.Y. Zhu, C. Song, G.Q. Shan, P. Chen, Characterization of photocatalyst Bi<sub>3.84</sub>W<sub>0.16</sub>O<sub>6.24</sub> and its photodegradation on bisphenol A under simulated solar light irradiation, *Appl. Catal. B: Environ.* 105 (2011) 229–236.
- [8] J.J. Mucia, M.C. Hidalgo, J.A. Navio, Study of the phenol photocatalytic degradation over TiO<sub>2</sub> modified by sulfation, fluorination, and platinum nanoparticles photodeposition, *Appl. Catal. B: Environ.* 179 (2015) 305–312.
- [9] A.V. Prasada Rao, A.I. Robin, S. Komarneni, Bismuth titanate from nanocomposite and sol-gel processes, *Mater. Lett.* 28 (1996) 469–473.
- [10] Y. Liu, M.Y. Zhang, L. Li, X.T. Zhang, One-dimensional visible-light-driven bifunctional photocatalysts based on Bi<sub>4</sub>Ti<sub>3</sub>O<sub>12</sub> nanofiber frameworks and Bi<sub>2</sub>XO<sub>6</sub> (X = Mo, W) nanosheets, *Appl. Catal. B: Environ.* 160–161 (2014) 757–766.
- [11] H.J. Zhang, G. Chen, X. Li, Synthesis and visible light photocatalysis water splitting property of chromium-doped Bi<sub>4</sub>Ti<sub>3</sub>O<sub>12</sub>, *Solid State Ion.* 180 (2009) 1599–1603.
- [12] H.Q. He, J. Yin, Y.X. Li, Y. Zhang, H.S. Qiu, J.B. Xu, T. Xu, C.Y. Wang, Size controllable synthesis of single-crystal ferroelectric Bi<sub>4</sub>Ti<sub>3</sub>O<sub>12</sub> nanosheet dominated with {001} facets toward enhanced visible-light-driven photocatalytic activities, *Appl. Catal. B: Environ.* 156–157 (2014) 35–43.
- [13] Z.W. Chen, H. Jiang, W.L. Jin, C.K. Shi, Enhanced photocatalytic performance over Bi<sub>4</sub>Ti<sub>3</sub>O<sub>12</sub> nanosheets with controllable size and exposed {001} facets for Rhodamine B degradation, *Appl. Catal. B: Environ.* 180 (2016) 698–706.
- [14] W.F. Yao, H. Wang, X.H. Xu, S.X. Shang, Y. Hou, Y. Zhang, M. Wang, Synthesis and photocatalytic property of bismuth titanate Bi<sub>4</sub>Ti<sub>3</sub>O<sub>12</sub>, *Mater. Lett.* 57 (2003) 1899–1902.
- [15] Y. Liu, M.Y. Zhang, L. Li, X.T. Zhang, In situ ion exchange synthesis of the Bi<sub>4</sub>Ti<sub>3</sub>O<sub>12</sub>/Bi<sub>2</sub>S<sub>3</sub> heterostructure with enhanced photocatalytic activity, *Catal. Commun.* 60 (2015) 23–26.
- [16] H.P. Zhang, M.K. Lü, S.W. Liu, L.Y. Wang, Z.L. Xiu, Y.Y. Zhou, Z.F. Qiu, A.Y. Zhang, Q. Ma, Preparation and photocatalytic property of perovskite Bi<sub>4</sub>Ti<sub>3</sub>O<sub>12</sub> films, *Mater. Chem. Phys.* 114 (2009) 716–721.
- [17] Y. Yalcin, M. Kilic, Z. Cinar, Fe<sup>3+</sup>-doped TiO<sub>2</sub>: A combined experimental and computational approach to the evaluation of visible light activity, *Appl. Catal. B: Environ.* 99 (2010) 469–477.
- [18] H.X. Li, X.Y. Zhang, Y.N. Huo, J. Zhu, Supercritical preparation of a highly active S-doped TiO<sub>2</sub> photocatalyst for methylene blue mineralization, *Environ. Sci. Technol.* 41 (2007) 4410–4414.
- [19] M.J. Zhou, D.L. Han, X.L. Liu, C.C. Ma, H.Q. Wang, Y.F. Tang, P.W. Huo, W.D. Shi, Y.S. Yan, Enhanced visible light photocatalytic activity of alkaline earth metal ions-doped CdSe/rGO photocatalysts synthesized by hydrothermal method, *Appl. Catal. B: Environ.* 172–173 (2015) 174–184.
- [20] H. Irie, K. Kamiya, T. Shibanuma, S. Miura, D.A. Tyrk, T. Yokoyama, K. Hashimoto, Visible light-sensitive Cu(II)-grafted TiO<sub>2</sub> photocatalysts:

activities and X-ray absorption fine structure analyses, *J. Phys. Chem. C* 113 (2009) 10761–10766.

[21] A.Z. Simoes, B.D. Stojanovic, M.A. Ramirez, A.A. Cavalheiro, E. Longo, J.A. Varela, Lanthanum-doped  $\text{Bi}_4\text{Ti}_3\text{O}_{12}$  prepared by the soft chemical method: rietveld analysis and piezoelectric properties, *Ceram. Int.* 34 (2008) 257–261.

[22] J.G. Hou, R. Cao, Z. Wang, S.Q. Jiao, H.M. Zhu, Chromium-doped bismuth titanate nanosheets as enhanced visible-light photocatalysts with a high percentage of reactive {110} facets, *J. Mater. Chem.* 21 (2011) 7296–7301.

[23] W.F. Yao, H. Wang, S.X. Shang, X.H. Xu, X.N. Yang, Y. Zhang, M. Wang, Photocatalytic property of Zn-modified bismuth titanate, *J. Mol. Catal. A: Chem.* 198 (2003) 343–348.

[24] X. Lin, Q.F. Gua, C.J. Zou, T.T. Liu, Y. Zhang, C.B. Liu, H.J. Zhai, Photocatalytic degradation of an azo dye using  $\text{Bi}_{3.25}\text{M}_{0.75}\text{Ti}_3\text{O}_{12}$  nanowires ( $\text{M} = \text{La}, \text{Sm Nd}$ , and Eu), *Mater. Sci. Eng. B* 178 (2013) 520–526.

[25] C.J. Huang, J.L. Hua, S. Cong, Z.G. Zhao, X.Q. Qiu, Hierarchical  $\text{BiOCl}$  microflowers with improved visible-light-driven photocatalytic activity by Fe(III) modification, *Appl. Catal. B: Environ.* 174–175 (2015) 105–112.

[26] M. Nussbaum, N. Shaham-Waldmann, Y. Paz, Synergistic photocatalytic effect in Fe, Nb-doped  $\text{BiOCl}$ , *J. Photochem. Photobiol. A: Chem.* 290 (2014) 11–21.

[27] X.H. Wu, W. Qin, L. Li, Y. Guo, Z.Y. Xie, Photocatalytic property of nanostructured Fe<sup>3+</sup>-doped  $\text{Bi}_2\text{O}_3$  films, *Catal. Commun.* 10 (2009) 600–604.

[28] S. Guo, X.F. Li, H.Q. Wang, F. Dong, Z.B. Wu, Fe-ions modified mesoporous  $\text{Bi}_2\text{WO}_6$  nanosheets with high visible light photocatalytic activity, *J. Colloid Interface Sci.* 369 (2012) 373–380.

[29] S. Chala, K. Wetchakun, S. Phanichphant, B. Inceesungvorn, N. Wetchakun, Enhanced visible-light-response photocatalytic degradation of methylene blue on Fe-loaded  $\text{BiVO}_4$  photocatalyst, *J. Alloys Compd.* 597 (2014) 129–135.

[30] G.R. Bamwenda, S. Tsubota, T. Nakamura, M. Haruta, Photoinduced hydrogen production from an aqueous solution of ethylene glycol over ultrafine gold supported on  $\text{TiO}_2$ , *J. Photochem. Photobiol. A* 77 (1994) 59–67.

[31] S.H. Nam, H.S. Shim, J.G. Kim, W.B. Kim, Ag or Au nanoparticle-embedded one-dimensional composite  $\text{TiO}_2$  nanofibers prepared via electrospinning for use in lithium-ion batteries, *ACS Appl. Mater. Interfaces* 2 (2010) 2046–2052.

[32] A. Dawson, P.V. Kamat, Semiconductor-metal nanocomposites photoinduced fusion and photocatalysis of Gold-capped  $\text{TiO}_2$  ( $\text{TiO}_2/\text{Gold}$ ) Nanoparticles, *J. Phys. Chem. B* 105 (2001) 960–966.

[33] Z. Wang, L. Zang, X.Y. Fan, H.Z. Jia, L. Li, W.Y. Deng, C.Y. Wang, Defect-mediated of Cu@ $\text{TiO}_2$  core-shell nanoparticles with oxygen vacancies for photocatalytic degradation 2,4-DCP under visible light irradiation, *Appl. Surf. Sci.* 358 (2015) 479–484.

[34] J.Q. Jiao, Y.C. Wei, Z. Zhao, W.J. Zhong, J. Liu, J.M. Li, A.J. Duan, G.Y. Jiang, Synthesis of 3D ordered macroporous  $\text{TiO}_2$ -supported Au nanoparticle photocatalysts and their photocatalytic performances for the reduction of  $\text{CO}_2$  to methane, *Catal. Today* 258 (2015) 319–326.

[35] G.Q. Zhu, W.X. Que, J. Zhang, Synthesis and photocatalytic performance of Ag-loaded-Bi<sub>2</sub>O<sub>3</sub> microspheres under visible light irradiation, *J. Alloys Compd.* 509 (2011) 9479–9486.

[36] K. Tian, W.J. Liu, H. Jiang, Comparative investigation on photoreactivity and mechanism of biogenic and chemosynthetic Ag/C<sub>3</sub>N<sub>4</sub> composites under visible light irradiation, *ACS Sustain. Chem. Eng.* 3 (2015) 269–276.

[37] H.Y. Li, Y.J. Sun, B. Cai, S.Y. Gan, D.X. Han, L. Niu, T.S. Wu, Hierarchically Z-scheme photocatalyst of Ag@AgCl decorated on  $\text{BiVO}_4$  (040) with enhancing photoelectrochemical and photocatalytic performance, *Appl. Catal. B: Environ.* 170–171 (2015) 206–214.

[38] J. Ren, W.Z. Wang, S.M. Sun, L. Zhang, J. Chang, Enhanced photocatalytic activity of Bi<sub>2</sub>WO<sub>6</sub> loaded with Ag nanoparticles under visible light irradiation, *Appl. Catal. B: Environ.* 92 (2009) 50–55.

[39] Y.N. Zhang, H.Q. Fan, M.M. Li, H.L. Tian, Ag/BiPO<sub>4</sub> heterostructures: synthesis, characterization and their enhanced photocatalytic properties, *Dalton Trans.* 42 (2013) 13172–13178.

[40] A. Pearson, H.D. Zheng, K. Kalantar-zadeh, S.K. Bhargava, V. Bansal, Decoration of  $\text{TiO}_2$  nanotubes with metal nanoparticles using polyoxometalate as a UV-switchable reducing agent for enhanced visible and solar light photocatalysis, *Langmuir* 28 (2012) 14470–144705.

[41] Y.C. Pu, G.M. Wang, K.D. Chang, Y.C. Ling, Y.K. Lin, B.C. Fitzmorris, C.M. Liu, X.H. Lu, Y.X. Tong, J.Z. Zhang, Y.J. Hsu, Y. Li, Au nanostructure-decorated  $\text{TiO}_2$  nanowires exhibiting photoactivity across entire UV-visible region for photoelectrochemical water splitting, *Nano Lett.* 13 (2013) 3817–3823.

[42] L. Jin, G.Q. Zhu, M. Hojamberdiev, X.C. Luo, J.H. Peng, P. Liu, A plasmonic Ag-AgBr/Bi<sub>2</sub>O<sub>3</sub> composite photocatalyst with enhanced visible-light photocatalytic activity, *Ind. Eng. Chem. Res.* 53 (2014) 13718–13727.

[43] Z.T. Hu, S.K. Lua, T.T. Lim, Cuboid-like  $\text{Bi}_2\text{Fe}_4\text{O}_9/\text{Ag}$  with graphene-wrapping tribrid composite with superior capability for environmental decontamination: nanoscaled material design and visible-light-driven multifunctional catalyst, *ACS Sustain. Chem. Eng.* 3 (2015) 2726–2736.

[44] L. Liu, S.L. Lin, J.S. Hu, Y.H. Liang, W.Q. Cui, Growth of nano Ag@AgCl on (111) facets of  $\text{Cu}_2\text{O}$  microcrystals with an enhanced photocatalytic activity, *RSC Adv.* 5 (2015) 62306–62313.

[45] J. Liang, G.Q. Zhu, P. Liu, X.C. Luo, C.W. Tan, L. Jin, J.P. Zhou, Synthesis and characterization of Fe-doped  $\beta$ -Bi<sub>2</sub>O<sub>3</sub> porous microspheres with enhanced visible light photocatalytic activity, *Superlattice Microstruct.* 72 (2014) 272–282.

[47] B.X. Wang, W.J. An, L. Liu, W. Chen, Y.H. Liang, W.Q. Cui, Novel Cu<sub>2</sub>S quantum dots coupled flower-like BiOBr for efficient photocatalytic hydrogen production under visible light, *RSC Adv.* 5 (2015) 3224–3231.

[48] H.G. Yu, G.Q. Cao, F. Chen, X.F. Wang, J.G. Yu, M. Lei, Enhanced photocatalytic performance of Ag<sub>3</sub>PO<sub>4</sub> by simultaneous loading of Ag nanoparticles and Fe(III) cocatalyst, *Appl. Catal. B: Environ.* 160–161 (2014) 658–665.

[49] Q. Fu, H. Saltsburg, M. Flytzani-Stephanopoulos, Active nonmetallic Au and Pt species on Ceria-based water-gas shift catalysts, *Science* 301 (2003) 935–938.

[50] Y. Wang, H.B. Fang, Y.Z. Zheng, R.Q. Ye, X. Tao, J.F. Chen, Controllable assembly of well-defined monodisperse Au nanoparticles on hierarchical  $\text{ZnO}$  microspheres for enhanced visible-light-driven photocatalytic and antibacterial activity, *Nanoscale* 7 (2015) 19118–19128.

[51] Y.M. Wu, J.L. Zhang, L. Xiao, F. Chen, Preparation and characterization of  $\text{TiO}_2$  photocatalysts by Fe<sup>3+</sup> doping together with Au deposition for the degradation of organic pollutants, *Appl. Catal. B: Environ.* 88 (2009) 525–532.

[52] S.K. Lee, A. Mills, Platinum and palladium in the semiconductor photocatalytic systems, *Platin. Met. Rev.* 47 (2003) 61–72.

[53] K. Inumaru, M. Murashima, T. Kasahara, S. Yamamoto, Enhanced photocatalytic decomposition of 4-nonylphenol by surface-organografted  $\text{TiO}_2$ : a combination of molecular selective adsorption and photocatalysis, *Appl. Catal. B: Environ.* 52 (2004) 275–280.

[54] S.J. Liang, R.W. Liang, L.R. Wen, R.S. Yuan, L. Wu, X.Z. Fu, Molecular recognitive photocatalytic degradation of various cationic pollutants by the selective adsorption on visible light-driven SnNb<sub>2</sub>O<sub>6</sub> nanosheet photocatalyst, *Appl. Catal. B: Environ.* 125 (2012) 103–110.

[55] S.J. Liang, S.Y. Zhu, Y. Chen, W.M. Wu, X.C. Wang, L. Wu, Rapid template-free synthesis and photocatalytic performance of visible light activated SnNb<sub>2</sub>O<sub>6</sub> nanosheets, *J. Mater. Chem.* 22 (2012) 2670–2678.

[56] L.Q. Jing, Y.C. Qu, B.Q. Wang, S.D. Li, B.J. Jiang, L.B. Yang, W. Fu, H.G. Fu, J.Z. Sun, Review of photoluminescence performance of nano-sized semiconductor materials and its relationships with photocatalytic activity, *Sol. Energy Mater. Sol. Cells* 90 (2006) 1773–1787.

[57] S.C. Warren, E. Thimsen, Plasmonic solar water splitting, *Energy Environ. Sci.* 5 (2012) 5133–5146.

[58] M.J. Kale, T. Avanesian, P. Christopher, Direct photocatalysis by plasmonic nanostructures, *ACS Catal.* 4 (2014) 116–128.

[59] S.J. Peng, P.N. Zhu, S.G. Mhaisalkar, S. Ramakrishna, Self-supporting three-dimensional  $\text{ZnIn}_2\text{S}_4/\text{PVDF-Poly(MMA-co-MAA)}$  composite mats with hierarchical nanostructures for high photocatalytic activity, *J. Phys. Chem. C* 116 (2012) 13849–13857.